Efficiency of Turbulent Reacceleration by Solenoidal Turbulence and Its Application to the Origin of Radio Megahalos in Cluster Outskirts

Kosuke Nishiwaki[1] , Gianfranco Brunetti[2] , Franco Vazza[2,3,4] , and Claudio Gheller[2]
[1] Institute for Cosmic Ray Research, The University of Tokyo, 5-1-5 Kashiwanoha, Kashiwa, Chiba 277-8582, Japan
[2] INAF Istituto di Radioastronomia, Via P. Gobetti 101, I-40129 Bologna, Italy
[3] Dipartimento di Fisica e Astronomia, Universita di Bologna, Via Gobetti 93/2, I-40129 Bologna, Italy
[4] Hamburger Sternwarte, Universität Hamburg, Gojenbergsweg 112, D-41029 Hamburg, Germany

Abstract

Recent radio observations with the Low Frequency Array (LOFAR) discovered diffuse emission extending beyond the scale of classical radio halos. The presence of such megahalos indicates that the amplification of the magnetic field and acceleration of relativistic particles are working in the cluster outskirts, presumably due to the combination of shocks and turbulence that dissipate energy in these regions. Cosmological magnetohydrodynamical (MHD) simulations of galaxy clusters suggest that solenoidal turbulence has a significant energy budget in the outskirts of galaxy clusters. In this paper, we explore the possibility that this turbulence contributes to the emission observed in megahalos through second-order Fermi acceleration of relativistic particles and magnetic field amplification by the dynamo. We focus on the case of A2255 and find that this scenario can explain the basic properties of the diffuse emission component that is observed under assumptions that are used in previous literature. More specifically, we conduct a numerical follow-up, solving the Fokker–Planck equation by using a snapshot of an MHD simulation and deducing the synchrotron brightness integrated along the lines of sight. We find that a volume-filling emission, ranging between 30% and almost 100% of the projected area, depending on our assumptions on the particle diffusion and transport, can be detected at LOFAR sensitivities. Assuming a magnetic field $B \sim 0.2~\mu G$, as derived from a dynamo model applied to the emitting region, we find that the observed brightness can be matched when $\sim 1\%$ of the solenoidal turbulent energy flux is channeled into particle acceleration.

Unified Astronomy Thesaurus concepts: Galaxy clusters (584)

1. Introduction

Galaxy clusters are filled with a hot intracluster medium (ICM) that has a characteristic temperature similar to the the cluster's virial temperature. This suggests that the ICM is heated by the gravitational energy released in the hierarchical merger and accretion processes of clusters (e.g., Press & Schechter 1974; Kravtsov & Borgani 2012). A fraction of the energy can also be channeled into nonthermal components, such as relativistic particles and magnetic fields. Shocks and turbulence could be favorable sites for the particle acceleration and the amplification of the field (see Brunetti & Jones 2014, for review).

Radio observations of galaxy clusters probe those non-thermal components by studying diffuse synchrotron emission of relativistic (cosmic-ray) electrons (CRes). A radio halo is a diffuse emission with an extent of ~ 1 Mpc, often found in the central region of merging clusters (see van Weeren et al. 2019, for review). The radiative cooling time of CRes is significantly shorter than the time required for diffusion or advection over ~ 1 Mpc, implying that there is an in situ mechanism that produces CRes. Reacceleration by merger-induced turbulence is the most plausible scenario (e.g., Brunetti et al. 2001; Petrosian 2001; Fujita et al. 2003; Cassano & Brunetti 2005), although cosmic-ray protons (CRps) in the ICM may be important ingredients in the physics of those phenomena (e.g.,

Dennison 1980; Blasi & Colafrancesco 1999). For example, they can provide seed CRes to reaccelerate through hadronic pp collisions with the thermal protons in the ICM (e.g., Brunetti & Lazarian 2011a; Brunetti et al. 2017; Pinzke et al. 2017; Nishiwaki & Asano 2022). It has been shown that the observed statistical properties of radio halos are in line with the reacceleration model considering the resonant interaction between compressible turbulence and relativistic particles (Cassano & Brunetti 2005; Nishiwaki & Asano 2022; Cassano et al. 2023). Reacceleration by turbulence is also proposed to explain radio emission detected on larger scales, such as radio bridges (Brunetti & Vazza 2020), which are radio filaments connecting massive pairs in the early stage of mergers discovered by the Low Frequency Array (LOFAR; Govoni et al. 2019; Botteon et al. 2020b).

More recently, Cuciti et al. (2022) reported the existence of radio "megahalos" in four clusters using LOFAR observations. The volume of the megahalos is almost 30 times larger than that of radio halos, suggesting that the entire volume of the cluster is filled with CRes and magnetic field. The radio power of megahalos is comparable to or even larger than that of classical halos. The detection of synchrotron radiation at a large distance (1–2 Mpc) from the cluster center also constrains the magnetic field strength in this region. Since the pressure of nonthermal components, including magnetic field and CRes, should be smaller than that of thermal ones, as indicated by the observations and numerical simulations (e.g., Vazza et al. 2016; Eckert et al. 2019), the magnetic field should be in the range $0.1~\mu G \lesssim B \lesssim 1.7~\mu G$ (Botteon et al. 2022). The lower bound ($0.1~\mu G$) is at least 1 order of magnitude larger than the

value expected from the compression of primordial fields. One possible mechanism for this nonlinear amplification of the field is a dynamo in a turbulent medium.

Cosmological simulations of galaxy clusters suggest that turbulence and shocks driven by continuous accretion of matter fill the entire volume of the cluster up to the virial radius (e.g., Vazza et al. 2011; Nelson et al. 2014; Miniati 2015; Steinwandel et al. 2023). As in the cluster center, the ICM in the outskirts is a weakly collisional plasma, and the perturbations would cause instabilities that effectively reduce the mean free path (mfp) of thermal protons (e.g., Schekochihin et al. 2005; Brunetti & Lazarian 2011b; Kunz et al. 2011), potentially establishing a well-developed inertial range (e.g., Schekochihin et al. 2009). Indeed, the infall of the clumps of mass drives the turbulence with a typical scale of a few hundred kiloparsecs in the cluster outskirts (e.g., Vazza et al. 2017). The timescale of the turbulent cascade, $t_{\rm cas} \sim 600$ Myr (e.g., Brunetti & Lazarian 2007), is much shorter than the Hubble time, which allows the turbulent dynamo to work in that region.

Nowadays, the best-studied case of the cluster producing diffuse radio emission over the entire cluster volume is the case of A2255 (Botteon et al. 2022). A2255 is a nearby ($z = 0.0806$) cluster, and shows a complex dynamical state in optical and X-ray observations (e.g., Burns et al. 1995; Feretti et al. 1997; Yuan et al. 2003; Akamatsu et al. 2017; Golovich et al. 2019). The cluster is known to host a radio halo and radio relics, and they have been studied over a wide range of frequencies (e.g., Jaffe & Rudnick 1979; Feretti et al. 1997; Govoni et al. 2005; Pizzo et al. 2008; Pizzo & de Bruyn 2009; Botteon et al. 2020a).

More recently, LOFAR observations found that the cluster hosts diffuse emission extending over very large scales and enveloping the classical halo and relics (Botteon et al. 2022). Such emission is complex, showing a number of relic-like features embedded in a truly diffuse component, and a spectral index distribution between 40 and 144 MHz ranging from 0.6 to 2.5. The flat-spectrum emission is coincident with the radio relics located in the north and southwest parts of the cluster, while the steep emission is associated with the diffuse component.

In this paper, we attempt to explore the possibility that turbulence contributes to the observed emission via magnetic field amplification and particle reacceleration. We use a cosmological MHD simulation of a cluster to examine the turbulent and magnetic fields in the cluster outskirts. In Section 2, we describe the setup of the MHD simulation. In Section 3, we review the reacceleration model and claim that that is compatible with the observed spectrum of the megahalo. In Section 4, we numerically solve the Fokker–Planck (FP) equation, considering the distribution of turbulence and its projection along the line of sight. The limitations of our models are discussed in Section 5. Finally, we summarize the results in Section 6.

2. Cosmological MHD Simulation

To examine the properties of the ICM and turbulence in cluster outskirts, we use a snapshot of a high-resolution cosmological ideal MHD simulation of a massive galaxy cluster, produced with grid code ENZO (Bryan et al. 2014). We use the same simulated cluster as in Botteon et al. (2022), which has a mass of $M_{200} = 8.65 \times 10^{14} M_\odot$ at $z = 0$. This

simulation includes eight levels of adaptive mesh refinement to increase the spatial and force resolution within the virial volume of the cluster, reaching a peak spatial resolution of $\Delta x = 3.95$ kpc/cell (comoving) (Vazza et al. 2018).

The simulation was started assuming a uniform "primordial" seed magnetic field of $B_0 = 0.1$ nG (comoving) at $z = 40$. The low-redshift properties of the magnetic field in the cluster volume are found to be fairly independent of the exact origin scenario, due to the effect of efficient small-scale dynamo amplification (Vazza et al. 2018). At the late stage of the cluster evolution, most of the central volume within <1 Mpc is simulated with the finest resolution $\Delta x = 3.95$ kpc/cell. The virial volume of clusters is refined at least up to $\Delta x = 15.8$ kpc/cell (Domínguez-Fernández et al. 2019). At 1–2 Mpc from the center, the spatial resolution is comparable to, or coarser than, the MHD scale, $l_{\rm A} \sim 1$ kpc, where the turbulent velocity becomes comparable to the Alfvén velocity, so the field amplification may be underestimated in the simulation. Thus, we evaluate the field strength in this region in a post-process (see Section 3 for the detail).

The turbulent kinetic flux is calculated with small-scale filtering explained in Vazza et al. (2017), which allows us to reconstruct (and remove) the contribution from shock waves to the total turbulent energy budget. For each cell of the simulation, the dispersion of the velocity field $\sigma_v(L)$ is measured within a scale L. The outer scale of the turbulence Λ is defined as the scale where the change in $\sigma_v(L)$ with increasing L becomes sufficiently small (see Vazza et al. 2017, for the detail). The turbulent kinetic energy flux in each simulated cell can be calculated as

$$\mathcal{F}_{\rm turb} = \frac{1}{2} \frac{\rho \sigma_v^3(L)}{L} (\Delta x)^3, \qquad (1)$$

where ρ is the gas mass density in the cell and Δx is the cell size. Based on previous works, we assume that the turbulent spectrum in the inertial range roughly follows the Kolmogorov scaling (e.g., Vazza et al. 2011, 2017), and so the value of $\mathcal{F}_{\rm turb}$ is insensitive to the specific value of L as long as it is in the inertial range. To study the quantities in the cluster outskirts, we extract a box that is 1.6 Mpc on a side located 1.2 Mpc from the center of the simulated cluster. Each cell has a volume of 16^3 kpc^3, and the box is composed of 10^6 cells. In this region, the outer scale Λ is found to be typically $\Lambda \approx 200$ kpc. In the following, we use the turbulent velocity measured at $L = 160$ kpc.

Figure 1 gives a visual impression of the line-of-sight gas velocity and of the gas temperature in the volume of the simulated clusters, in particular in the box used to extract the physical parameters used in our Fokker–Planck calculations. The selected box is at the cluster periphery, in a region only partially detectable through typical X-ray observations, and in the direction of a prominent filamentary accretion, but without the presence of massive substructures or prominent shock waves.

Figure 2 (left panel) shows a histogram of turbulent kinetic flux in the extracted region. We decompose the turbulent velocity into solenoidal ($\nabla \cdot \boldsymbol{v} = 0$) and compressible ($\nabla \times \boldsymbol{v} = 0$) modes, using the procedure of Vazza et al. (2017). We find that the solenoidal mode typically has a larger kinetic flux than the compressible mode, in line with previous simulations (e.g., Miniati 2015; Porter et al. 2015; Vazza et al. 2017). The mean value of the solenoidal
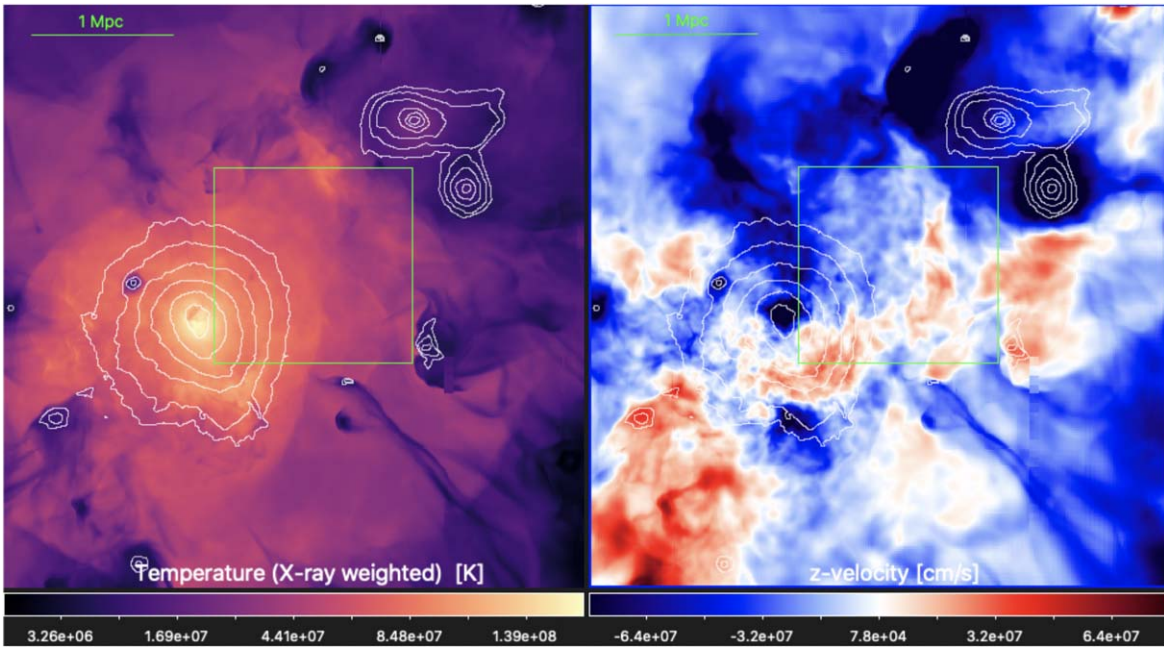
Figure 1. Maps of the X-ray-weighted gas temperature along the line of sight (left) and of the gas velocity along the line of sight (right) for the simulation snapshot analyzed in this work. The additional white contours show the regions that can be approximately detected with X-ray observations in the 0.5–2 keV energy band, while the green square shows the location of the box used to extract the turbulent flow properties used in Section 4. Each image is made of 1024×1024 pixels.
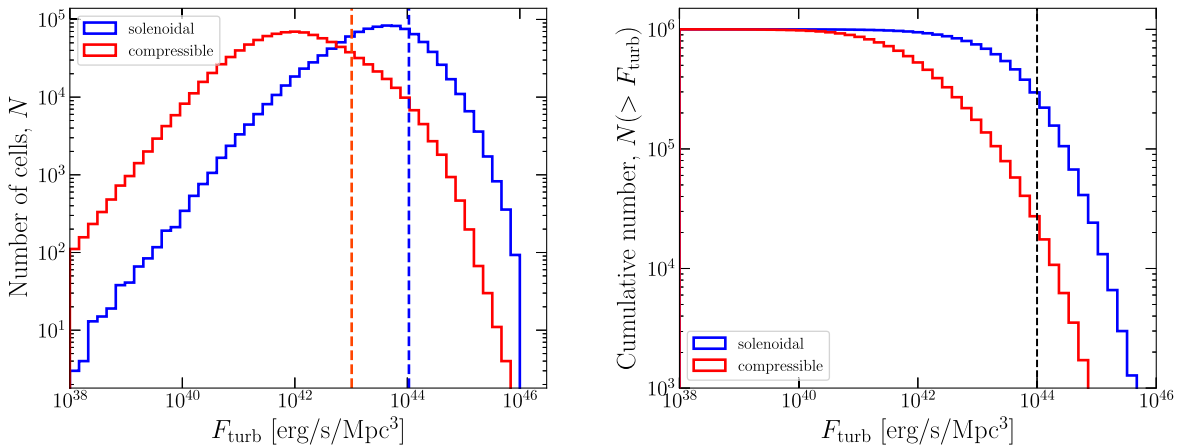

Figure 2. Left: histogram of turbulent energy flux per unit volume for solenoidal (blue) and compressible (red) modes in the cluster peripheral region shown in Figure 1. The vertical axis shows the number of cells in the simulated box. The dotted vertical lines show the mean values for each mode. The total number of cells in the extracted box is $N = 10^6$. Right: cumulative number of cells with turbulent kinetic flux larger than F_{turb}. The vertical dashed line shows $F_{\mathrm{turb}} = 10^{44}$ erg s^{-1} Mpc^{-3}.

kinetic flux per unit volume is $F_{\mathrm{turb}} = 1.1 \times 10^{44}$ erg s^{-1} Mpc^{-3}, which is almost 10 times as large as the compressible component. In the right panel, we show the cumulative number of cells that have turbulent kinetic flux larger than F_{turb}. More than 30% of the cells have the solenoidal turbulent flux larger than 10^{44} erg s^{-1} Mpc^{-3}, while the fraction decreases to $\approx$3% in the case of the compressible mode. Note that we are considering the sector where the feature of mass accretion from the nearby cluster can be seen (Figure 1) and it is more turbulent than other sectors of the cluster outskirts (see also Section 5). For comparison, we study other regions with the same volume and distance from the cluster center and find a turbulent flux a factor $\sim$5 smaller, whereas the solenoidal mode dominates the compressible one in every region. In the following sections, we focus on the solenoidal velocity to calculate the acceleration efficiency and the dynamo field. Note that F_{turb} denotes only the volumetric turbulent kinetic flux of the solenoidal component.

3. CR Reacceleration and Field Amplification by Solenoidal Turbulence

Turbulence driven through the formation process of galaxy clusters is typically subsonic ($M_{\mathrm{s}} < 1$) and super-Alfvénic ($M_{\mathrm{A}} > 1$) (Brunetti & Lazarian 2007). A fraction of the turbulent energy can be converted into nonthermal components such as cosmic rays and the magnetic field through stochastic acceleration and a turbulent dynamo. Turbulence in astrophysical environments may accelerate particles via different mechanisms, including resonant and nonresonant ones (e.g., Ptuskin 1988; Schlickeiser & Miller 1998; Cho & Lazarian 2006; Brunetti & Lazarian 2007;2016; Lynn et al. 2014; Lemoine 2021; Bustard & Oh 2022; Lazarian & Xu 2023). Recent MHD simulations of galaxy clusters suggested that the turbulence in the ICM is dominated by the solenoidal (incompressible) mode (e.g., Miniati 2015; Vazza et al. 2017). One possible acceleration mechanism working in

incompressible turbulence is the acceleration due to the interaction between magnetic field and particles diffusing in super-Alfvénic turbulence (Brunetti & Lazarian 2016; Brunetti & Vazza 2020).

In turbulent reconnection theory (Lazarian & Vishniac 1999), the Alfvén scale $l_{\rm A} \equiv L M_{\rm A}^{-3}$ (for the Kolmogorov scaling) is the dominant scale, where the reconnection speed may reach $v_{\rm rec} \sim v_{\rm A}$. In the regions where the magnetic field dissipates due to the reconnection, the particles trapped in contracting islands gain energy through a mechanism that is similar to the first-order Fermi mechanism (Kowal et al. 2012; del Valle et al. 2016). In contrast, the particles are expected to cool in the regions where the dynamo is efficient and the magnetic field lines diverge.

According to Brunetti & Lazarian (2016), particles diffusing through this complex pattern experience a second-order acceleration mechanism. In this mechanism, the diffusion coefficient in the momentum space is

$$D_{pp} = 3\sqrt{\frac{5}{6}}\frac{c_s^2}{c}\frac{\sqrt{\beta_{\rm pl}}}{L}M_s^3\psi^{-3}p^2, \tag{2}$$

where p is the momentum of the particle, $\beta_{\rm pl} \equiv 2\gamma_{\rm ad}^{-1}c_{\rm s}^2/v_{\rm A}^2$ is the plasma beta with $\gamma_{\rm ad} = 5/3$ the adiabatic index, and $\psi \equiv \lambda_{\rm mfp}/l_{\rm A}$ with $\lambda_{\rm mfp}$ the mfp of the particle. The mfp is an important parameter in the model as it determines the spatial diffusion coefficient,

$$D \sim \frac{1}{3}c\lambda_{\rm mfp} \sim 10^{31}\,{\rm cm^2\,s^{-1}}\left(\frac{\psi}{0.5}\right)\left(\frac{l_{\rm A}}{1\,{\rm kpc}}\right), \tag{3}$$

and consequently the efficiency of a particle crossing regions of size $l_{\rm A}$. Combining the requirement that the fractional change of momentum in each scattering should be $\Delta p/p \ll 1$ and the effect of particle scattering due to mirroring in a super-Alfvénic flow, ψ should satisfy $0.01 \ll \psi \lesssim 0.5$; $\psi \sim 0.5$ is the reference value that has been motivated and used in previous studies (Brunetti & Lazarian 2016; Brunetti & Vazza 2020).

We consider that the solenoidal turbulence with super-Alfvénic injection velocity shows a power spectrum with a well-established inertial range. In such a situation, a fixed fraction ($\eta_B \approx 0.05$) of the turbulent energy flux is consumed through amplification of the magnetic field (e.g., Cho et al. 2009; Beresnyak 2012; Xu & Lazarian 2016). MHD simulations of galaxy clusters succeed in resolving the small-scale turbulent dynamo in the central region (e.g., ZuHone et al. 2011; Vazza et al. 2018; Domínguez-Fernández et al. 2019; Steinwandel et al. 2022), but this effect is quenched in the cluster periphery due to the limited resolution. Thus, we adopt the same procedure as Brunetti & Vazza (2020) and estimate the dynamo-amplified field in post-processing, in the output of the MHD simulation (Section 2). Assuming that a fraction η_B of the turbulent kinetic energy is channeled into the field amplification, the field strength can be estimated as

$$\frac{B^2}{8\pi} \sim \eta_B F_{\rm turb} t_{\rm eddy} \sim \frac{1}{2}\eta_B \rho_{\rm ICM}\delta v_{\rm turb}^2, \tag{4}$$

where $t_{\rm eddy} = L/\delta v_{\rm turb}$ is the eddy turnover time. In this case, $M_{\rm A}$ and η_B are related as $M_{\rm A} \sim \eta_B^{-1/2}$. In the simulations of galaxy clusters, the value of η_B is as small as $\eta_B \approx 0.05$ (Beresnyak & Miniati 2016; Vazza et al. 2018). Using $\eta_B = 0.05$, we obtain the mean field strength of

$\langle B \rangle \sim 0.24\,\mu{\rm G}$ in the simulated box, which is more than twice as large as the mean value of the field strength directly measured in the simulation ($\langle B_{\rm sim}\rangle = 0.11\,\mu{\rm G}$). The plasma beta is $\beta_{\rm pl} \approx 200$–500, which is slightly larger than that in the cluster center (e.g., Brunetti & Lazarian 2007). Adopting the dynamo field (Equation (4)), D_{pp} (Equation (2)) can be expressed as a function of η_B as (Brunetti & Vazza 2020)

$$D_{pp} \sim 3\frac{\delta v_{\rm turb}^2}{cL}\eta_B^{-1/2}\psi^{-3}p^2. \tag{5}$$

The spectral index map of A2255 in Botteon et al. (2022) is a mixture of flat ($\alpha_{\rm syn} \sim 1.0$) and steep ($\alpha_{\rm syn} \sim 2.0$) regions. The flattest index is coincident with the arc-shaped structure, suggesting particle energization by shocks. On the other hand, the emission with steep radio indices comes from the diffuse envelope permeating the cluster volume (see Figure S2 of Botteon et al. 2022). The mean value of the index is around $\alpha_{\rm syn} \approx 1.6$. If we assume a scenario where particles emit in a homogeneous field, those steep indices suggest that the observing frequency is close to the steepening frequency, at which the spectrum starts to decline rapidly due to the cooled spectrum of CRes.

In the turbulent reacceleration model of CRes, one can define the break energy $\gamma_{\rm b}$ as the energy where the cooling timescale $t_{\rm cool}$ becomes comparable to the acceleration timescale $t_{\rm acc}$. As shown in Cassano et al. (2010), the steepening frequency $\nu_{\rm s}$ in the synchrotron spectrum appears a factor $\xi \sim 5$–7 times higher than the break frequency $\nu_{\rm b}$ corresponding to $\gamma_{\rm b}$, i.e., $\nu_{\rm s} = \xi\nu_{\rm b}$. The cooling time of ultrarelativistic CRes due to synchrotron and inverse Compton (IC) radiation can be written as $t_{\rm cool} = 6\pi m_e c\gamma^{-1}/(\sigma_{\rm T}(B^2 + B_{\rm CMB}^2))$, where γ is the Lorentz factor of the particle, $\sigma_{\rm T}$ is the Thomson cross section, and $B_{\rm CMB} = 3.25(1 + z)^2\,\mu{\rm G}$ is the IC equivalent field. Note that 100 MHz emission is mainly produced by the synchrotron radiation of CRes with $p = \sqrt{\gamma^2 - 1} \sim 10^4$, and the Coulomb loss is negligible for those CRes. Using the magnetic field estimated from the dynamo model of Equation (4), the cooling timescale at $\nu_{\rm b}$ can be estimated as

$$t_{\rm cool} = \frac{\sqrt{27\pi e m_e c}}{\sigma_{\rm T}}\frac{B^{1/2}}{B^2 + B_{\rm CMB}^2}\xi^{1/2}\nu_{\rm s}^{-1/2},$$
$$\sim 450\,{\rm Myr}\left(\frac{\eta_B}{0.05}\right)^{1/4}(1+z)^{-5/2}\left(\frac{\mu}{0.59}\right)^{1/4}\left(\frac{n_{\rm ICM}}{10^{-4}\,{\rm cm^{-3}}}\right)^{1/4}$$
$$\times\left(\frac{\delta v_{\rm turb}}{300\,{\rm km\,s^{-1}}}\right)^{1/2}\left(\frac{\xi}{7}\right)^{1/2}\left(\frac{\nu_{\rm o}}{100\,{\rm MHz}}\right)^{-1/2}, \tag{6}$$

where μ is mean molecular weight and $\nu_{\rm o} = \nu_{\rm s}/(1 + z)$ is the observing frequency. The cooling is dominated by the radiation through the IC scattering ($B^2 \ll B_{\rm CMB}^2$) in the cluster outskirts, so we neglected the B^2 term in the denominator. The acceleration timescale should be comparable to this value to sustain the emission observed at the LOFAR frequency.

Comparing Equation (6) with the acceleration timescale $t_{\rm acc} = p^2/(4D_{pp})$ obtained from Equation (5), one can relate two fundamental parameters, ψ and η_B. Figure 3 shows the relation between η_B and ψ in the case of $\nu_{\rm o} = 50$ MHz and $z = 0$. We adopted the typical values for the ICM density and temperature in cluster outskirts: $n_{\rm ICM} = 3 \times 10^{-5}\,{\rm cm^{-3}}$ and $T_{\rm ICM} = 4$ keV. Adopting $\eta_B \sim 0.05$ and the typical turbulent flux found in MHD simulation, $F_{\rm turb} \approx 10^{44}\,{\rm erg\,s^{-1}\,Mpc^{-3}}$ (Figure 2), we find that the observed steep spectrum at LOFAR frequencies can be explained with the mfp of CRes $\psi \sim 0.5$ of the Alfvén scale.
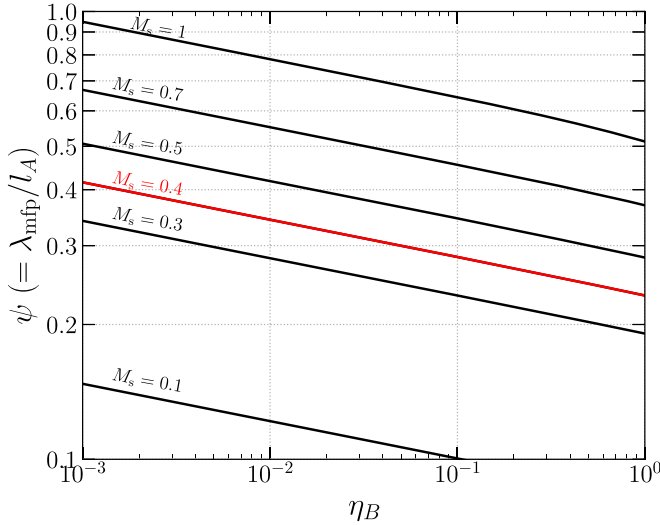
Figure 3. Relation between η_B and ψ, required for the observing frequency of $\nu_o = 50$ MHz and $\xi = 7$. Lines distinguish the results for the different turbulent velocities at $L = 0.16$ Mpc; $M_s = 0.1, 0.3, 0.4, 0.5, 0.7,$ and 1.0 (from bottom to top). For the ICM properties, we adopted typical values at the cluster periphery found in MHD simulations, $n_{ICM} = 3 \times 10^{-5}$ cm^{-3} and $T_{ICM} = 4$ keV. The source is assumed to be at $z = 0$.

This value is consistent with that adopted by Brunetti & Lazarian (2016) and Brunetti & Vazza (2020) to explain radio halos and bridges. The mfp comparable to l_A in turbulence reconnection is supported by the studies of tracers in MHD simulations (Kowal et al. 2011, 2012).[5]

One can calculate the number of cells that are important for the radio emission by comparing t_{acc} and t_{cool} measured in the extracted cubic volume. Using Equations (5) and (6), the scaling relation for the ratio of those timescales can be expressed as

$$\frac{t_{acc}}{t_{cool}} \propto \rho^{-1/4} \delta v_{turb}^{-5/2} L \xi^{-1/2} \psi^3 \eta_B^{1/4}, \quad (7)$$

In Figure 4, we show the cumulative fraction of t_{acc}/t_{cool}. When $t_{acc} < t_{cool}$, the acceleration mechanism of Equation (2) can efficiently reaccelerate CRes that radiate synchrotron emission at the LOFAR frequencies.

The fraction of cells is $\sim 15\%$ adopting a reference value $\psi = 0.5$, while it increases to $\gtrsim 50\%$ for $\psi < 0.2$–0.3. The dependence on η_B is rather weak (Equation (7)). The fraction ranges from 25% to 10% for $\eta_B = 0.01$–0.1, for a fixed $\psi = 0.5$. Such a significant fraction implies a volume-filling emission. One also needs to take care about the duration of reacceleration, since the reacceleration is important only when it lasts for several times longer than t_{acc}. The filling factor of the radio-emitting cells will be revisited in Section 4.

4. Fokker–Planck Simulation

Next, we study the synchrotron spectrum in our dynamo reacceleration model with a numerical calculation. We consider the situation in which the pre-existing population of seed CRes is reaccelerated by incompressible turbulence and produces the observed radio emission via synchrotron radiation. As in Section 2, we consider the volume of 1.6^3 Mpc^3 located
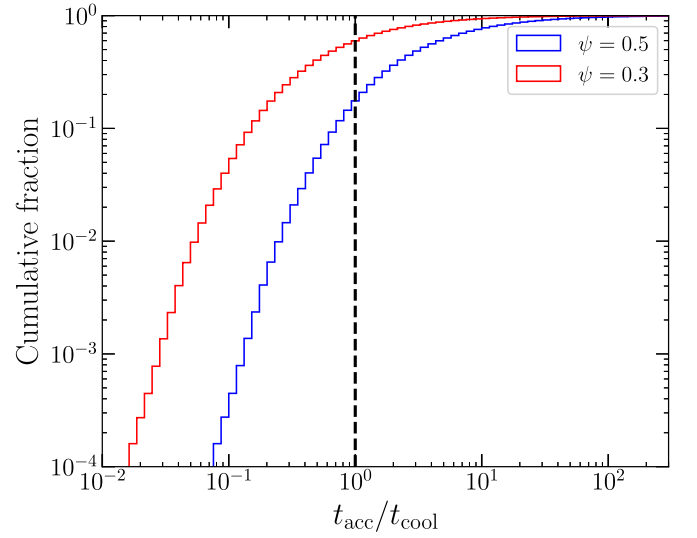
---

[5] More recent theoretical attempts have also investigated the role of mirroring in particle diffusion and acceleration (Lazarian & Xu 2021, 2023).


Figure 4. Cumulative number count of cells as a function of t_{acc}/t_{cool} in the case of $\psi = 0.3$ (red) and 0.5 (blue). We adopted the same parameters as Figure 3 ($\nu_o = 50$ MHz, $\xi = 7$, and $\eta_B = 0.05$). The vertical dotted line shows $t_{acc} = t_{cool}$.

1.2 Mpc from the center, and the distribution of the seed CRes is proportional to the ICM number density. We solve the Fokker–Planck equation for CRes in the following form (e.g., Cassano & Brunetti 2005):

$$\frac{\partial N_e(p, t)}{\partial t} = \frac{\partial}{\partial p}[\dot{p} N_e]$$
$$+ \frac{\partial}{\partial p}\left[D_{pp}\frac{\partial N_e}{\partial p} - \frac{2}{p}N_e D_{pp} \right] + Q_e(p, t), \quad (8)$$

where $N_e(p, t)$ is the spectrum of CRes at time t, $\dot{p}$ represents the momentum loss per unit time, D_{pp} is the momentum diffusion coefficient, and Q_e is the injection spectrum of CRes. The momentum loss rate $\dot{p}$ includes the effect of radiative (synchrotron and IC) and Coulomb losses, and D_{pp} is calculated with Equation (2). We neglect the injection of secondary electrons from inelastic pp collisions of CRps. Due to the low ICM density in the cluster outskirts, the contribution of the secondary electrons is expected to be smaller than that in classical radio halos (see Appendix A for further discussion).

We neglect the term related to the spatial transport of CRs in Equation (8), since it cannot be properly followed with a snapshot of the MHD simulation. However, we are considering the case where the mfp of CRes is comparable to the Alfvén scale ($l_A \sim 1$ kpc), and this leads to a large value of the spatial diffusion coefficient $D \sim 10^{31}$ cm^2 s^{-1}, as shown in Equation (3). A detailed investigation of the effect of spatial transport in the reacceleration model is left for future works using a Lagrangian tracer method. In this exploratory work, we adopt the following two approaches: a one-zone approximation (Section 4.1), where we adopt the average value of the physical quantities found in the snapshot, and a calculation considering the variation of F_{turb} in each cell and the integration along the line of sight (LOS; Section 4.2).

4.1. One-zone Calculation

We first discuss the energy density of CRes required to reproduce the observed emission under the one-zone
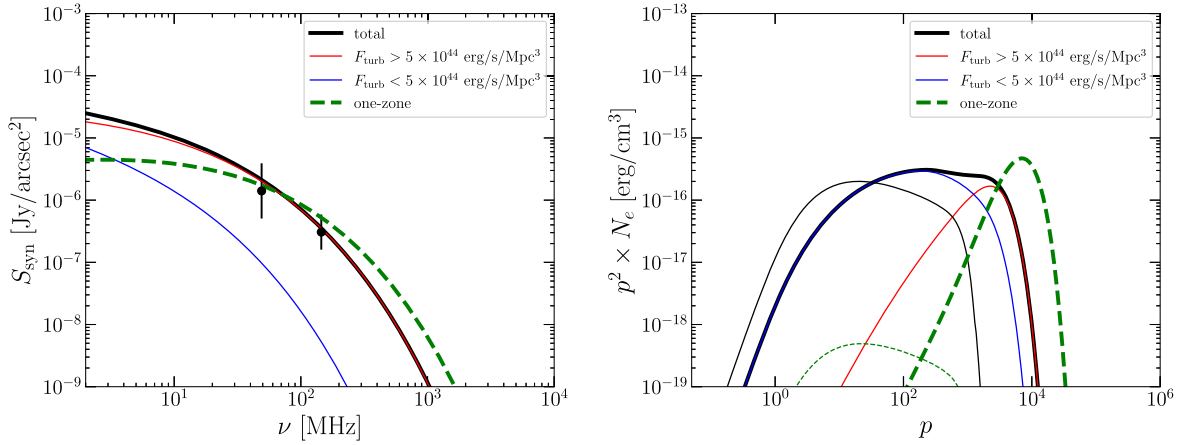
Figure 5. Left: the thick solid line shows the synchrotron spectrum in a single beam, typically seen in our calculation with 10^6 cells. For comparison, the spectrum in the one-zone model is shown as the dashed line. The data points show the typical value of the brightness measured at 1.5–2 Mpc from the cluster center (Botteon et al. 2022). The error bars show the ranges of the brightness in this region including 1σ error. We adopt $\psi = 0.3$ for the one-zone model, while $\psi = 0.6$ for the cell-wise calculations. In both models, we assume $T_{\mathrm{dur}} = 3$ Gyr. The beam spectrum is decomposed into the contributions from the cells with $F_{\mathrm{turb}} < 5 \times 10^{44}$ erg s^{-1} Mpc^{-3} (blue) and $F_{\mathrm{turb}} > 5 \times 10^{44}$ erg s^{-1} Mpc^{-3} (red). Right: CRe spectra in the same calculations. Spectra before and after the reacceleration are shown with thin and thick black lines, respectively. The dashed lines show the spectra in the one-zone model.

approximation. We adopt the mean values in the simulation box for the physical quantities: $n_{\mathrm{ICM}} = 6 \times 10^{-5}$ cm^{-3}, $T_{\mathrm{ICM}} = 4.5$ keV, $v_{\mathrm{sol}} = 320$ km s^{-1} ($M_s \approx 0.4$), and $t_{\mathrm{eddy}} = 0.53$ Gyr. We adopt $\eta_B = 0.05$, which corresponds to $B = 0.24\,\mu$G (Equation (4)). We summarize the values of parameters in Table 1. As an initial condition, a cooled spectrum of seed CRes is calculated by integrating Equation (8) for 2 Gyr with $D_{pp} = 0$ and $Q_e(p, t) \propto p^{-\alpha_{\mathrm{inj}}} \delta(t)$, where $\alpha_{\mathrm{inj}} = 2.2$ and $\delta(t)$ is the Dirac delta function. Due to the radiative and Coulomb cooling, the seed CRes have steep cutoffs around $p_{\mathrm{min}} \sim 10$ and $p_{\mathrm{max}} \sim 10^3$ (Figure 5, right panel). The normalization of the initial spectrum is treated as a free parameter.

As seen from Figure 3, for $M_s \sim 0.4$–0.7, a value $\psi \sim 0.3$–0.5 is compatible with the observed emission. This is confirmed by numerical calculation in Figure 5 (left panel), where we plot the synchrotron spectrum in the one-zone model with a dashed line. While the spectral shape is mainly determined by the parameters η_B and ψ (Equation (7)), the normalization (brightness) depends on the initial spectrum $N_e(p, 0)$ and the duration of reacceleration T_{dur}. In this section, we assume that T_{dur} is sufficiently long and the CRe spectrum reaches a steady state due to the balance between reacceleration and radiative cooling (Equation (8)). We find that this steady state is achieved at $T_{\mathrm{dur}} \geqslant 3$ Gyr. The duration of $T_{\mathrm{dur}} = 3$ Gyr is comparable to the dynamical timescale of the ICM in the simulated region, so the mean value of the turbulent flux F_{turb} can evolve in this timescale. Thus, the assumption of constant F_{turb} during the FP calculation should be considered as a rough approximation.

We determine the normalization of the initial spectrum as the synchrotron brightness at 49 MHz matches the observed value. The data points in Figure 5 show the range of the brightness of the diffuse envelope measured at 1.5–2 Mpc from the center of A2255 (Botteon et al. 2022).

We define the efficiency of the reacceleration, η_{acc}, as the fraction of the turbulent kinetic flux that turns into the increase in the CRe energy density and the radiation:

$$\eta_{\mathrm{acc}} F_{\mathrm{turb}} \equiv \frac{d\epsilon_{\mathrm{CRe}}}{dt} + \varepsilon_{\mathrm{rad}}, \qquad (9)$$

Table 1
Parameters Adopted in the FP Calculations

	Section 4.1	Section 4.2
ψ	0.3	0.6
η_B	0.05	0.05
T_{dur} [Gyr]	3	3
L [kpc]	160	160
F_{turb} [erg s^{-1} Mpc^{-3}]	1.1×10^{44}	...[a]
n_{ICM} [cm^{-3}]	6×10^{-5}	...[a]
T_{ICM} [keV]	4.5	...[a]
B [μG]	0.24[b]	...,[a b]

Notes.
[a] We use the values found each simulated cell.
[b] The magnetic field is calculated with Equation (4).

where ϵ_{CRe} is the CRe energy density and $\varepsilon_{\mathrm{rad}} = \varepsilon_{\mathrm{syn}} + \varepsilon_{\mathrm{IC}}$ is the sum of the frequency-integrated emissivities of synchrotron and IC radiations. In the steady state of N_e, the first term on the right-hand side is negligible. The synchrotron emissivity $\varepsilon_{\mathrm{syn}}$ is calculated in the range 10^4–10^{10} Hz, and $\varepsilon_{\mathrm{IC}}$ is calculated with $\varepsilon_{\mathrm{IC}} = (B_{\mathrm{cmb}}/B)^2 \times \varepsilon_{\mathrm{syn}}$. Since $B \ll B_{\mathrm{cmb}}$, $\varepsilon_{\mathrm{rad}}$ is dominated by $\varepsilon_{\mathrm{IC}}$.

In Figure 5 (dashed line), we show the CRe energy spectrum in the steady state. The energy is dominated by particles emitting at 100 MHz, and the particles with $p < 10^3$ are not energetically important. We find $\epsilon_{\mathrm{rad}} \approx 7 \times 10^{-30}$ erg s^{-1} cm^{-3} and $\eta_{\mathrm{acc}} \approx 2\%$, which are consistent with the estimate in Botteon et al. (2022). Due to the assumption of stationary conditions, this result is independent of the initial spectrum.

We find that the spectrum in Figure 5 is reasonably reproduced by considering a range of values of ψ around the reference value $\psi \sim 0.5$. On the other hand, the assumption of an mfp that is significantly reduced, $\psi < 0.2$, generates spectra that are too hard compared to the observation. Note that this result is based on the assumption that the turbulence and physical parameters in the simulated ICM are representative of the external regions in A2255.

4.2. Projection along the LOS

Next, we consider the distribution of turbulent energy in the box and study how the emission from highly turbulent cells affects the spectrum integrated along the LOS. To consider the CRe spectrum in each simulated cell, we calculate the FP equation for various F_{turb} found in the simulated box. We make a histogram of F_{turb} with 160 bins equally spaced on a logarithmic scale in the range 10^{38} erg s^{-1} Mpc^{-3} < F_{turb} < 10^{46} erg s^{-1} Mpc^{-3} (Figure 2). For simplicity, we adopt the same values of dynamo B (Equation (4)) and D_{pp} (Equation (5)) for the cells in the same F_{turb} by calculating the mean values of ρ_{ICM} and v_{turb} in each F_{turb} bin. The synchrotron brightness is calculated by integrating the emissivity of 100 cells (corresponding to 1.6 Mpc) along the axis of the simulation. In one projection, there are 100×100 LOSs.

We assume the same initial spectrum as in Section 4.1, i.e., the spectrum with cutoffs at $p_{min} \sim 10$ and $p_{max} \sim 10^3$. As in the previous section, we consider a sufficiently long $T_{dur} = 3$ Gyr to ensure that the steady state due to the balance between cooling and reacceleration is achieved in many of the cells. Note that the turbulent flux in each cell would change in a few eddy turnover times, with $t_{eddy} \sim 0.3$–1 Gyr. When T_{dur} is short and the steady state is not achieved, the result may depend on the initial condition. This point is further discussed in Appendix B, where we show that the observed emission can be explained with a different combination of T_{dur} and the initial condition.

The nondimensional parameters in our model, ψ (Equation (2)) and η_B (Equation (4)), are assumed to be constant over cells. As a test case, we adopt the same $\eta_B = 0.05$ as the one-zone calculation. We use a snapshot of the simulation and do not consider the evolution of the background fluid. We assume that the initial energy density of the CRes in each cell is proportional to the thermal energy density, i.e., $\epsilon_{CRe}(t = 0) \propto \epsilon_{ICM}$. We neglect the particle transport between cells during the calculation. Those simplifications reduce the computational cost and enable us to calculate the spectrum in every cell in the box for several gigayears. The study of the impact of CR transport is left to future works featuring the Lagrangian tracer approach (Section 5).

We calculate the distribution of the spectral index and compare it with the observation by Botteon et al. (2022). The spectral index and its statistical properties would depend on the beam size and sensitivity of the observation, so we consider those of LOFAR. The beam size in Botteon et al. (2022) is 35″, which corresponds to almost three times the cell size at the redshift of A2255, so we calculate the spectrum of one beam by summing up the intensities of 3×3 neighboring LOSs. Each simulated beam consists of the emission from 900 cells. Following Botteon et al. (2022), we introduce a cut in our simulated data, neglecting the beams that have 145 MHz brightness below $2\sigma_{HBA}$, where $\sigma_{HBA} = 200 \mu$Jy is the rms noise per beam of the LOFAR High Band Antenna (HBA) band.

In Figure 5, we show the typical synchrotron spectrum of a beam detectable with the LOFAR sensitivity (black); here we specifically use $\psi = 0.6$. Since more turbulent cells contribute more than less turbulent cells the results are not exactly consistent with those in the one-zone model (Section 4.1) or with Figure 3. In fact, the model considering the LOS integration of $\sim 10^3$ cells (in each beam) requires a slightly
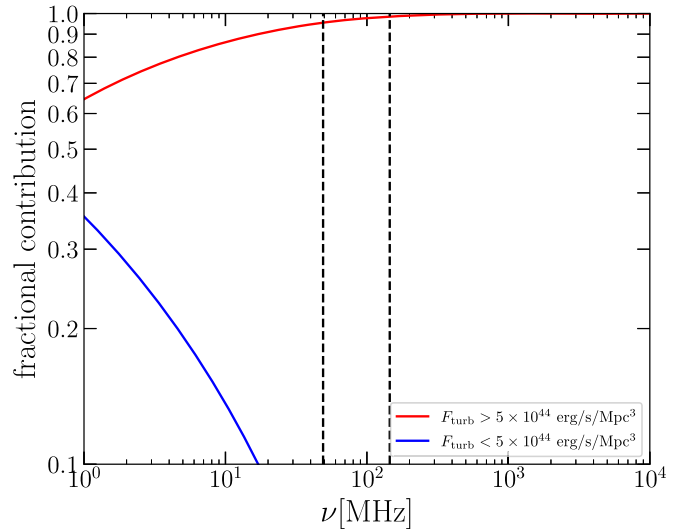

Figure 6. Fractional contribution from cells with $F_{turb} > 5 \times 10^{44}$ erg s^{-1} Mpc^{-3} (orange) and $F_{turb} < 5 \times 10^{44}$ erg s^{-1} Mpc^{-3} (blue) to the flux shown in Figure 5. The vertical dashed lines show the Low and High Band Antenna frequencies of LOFAR.

larger value of ψ and consequently a slightly less efficient acceleration mechanism.

We decompose the spectrum into the contributions from cells with $F_{turb} > 5 \times 10^{44}$ erg s^{-1} Mpc^{-3} (orange) and $F_{turb} < 5 \times 10^{44}$ erg s^{-1} Mpc^{-3} (blue). We confirm the trend seen in Brunetti & Vazza (2020); at higher frequencies ($\nu > 100$ MHz), the highly turbulent cells dominate the emission, which occupies only a small fraction (4.5%) of the volume, while the emission is more volume-filling at lower frequencies. In Figure 6, we show the contribution from the turbulent cells as a function of frequency. CRe spectra are compared in Figure 5. Unlike one-zone calculation, the overall spectrum has a bump around $p \sim 100$. CRes in the cells with smaller turbulent energy dominate the CRe energy, although they do not significantly contribute to the emission at ~ 100 MHz (Figure 6). The typical momentum of CRes that corresponds to 100 MHz emission shifts to $p \sim (2$–$5) \times 10^3$, since the magnetic field in cells with $F_{turb} \approx 5 \times 10^{44}$ erg s^{-1} Mpc^{-3} is a factor ~ 2 stronger than $B = 0.24 \mu$G adopted in the one-zone model. As discussed in Appendix B, the contribution from low F_{turb} can be larger and the emission becomes more volume-filling under a different assumption on the initial condition.

In reality, the CR distribution would be smoothed by diffusion and/or streaming, and CRs would experience multiple reaccelerations within the dynamical time. In such a situation, the gap between cells with large F_{turb} and small F_{turb} would be reduced and the emission would become more volume-filling. This point will be further studied in future with a Lagrangian tracer method (see also Section 5).

We find that 375 beams out of 1089 satisfy the criterion of detection, i.e., $S_{HBA} > 2\sigma_{HBA}$, so almost 34% of the area of the emission region can be covered by the LOFAR sensitivity. This fraction increases with the efficiency of reacceleration (smaller ψ), as the contribution from the less turbulent cells ($F_{turb} < 5 \times 10^{44}$ erg s^{-1} Mpc^{-3}) becomes more significant. However, we find that, for $\psi \lesssim 0.3$, the typical spectrum starts to become flatter than the observed one.
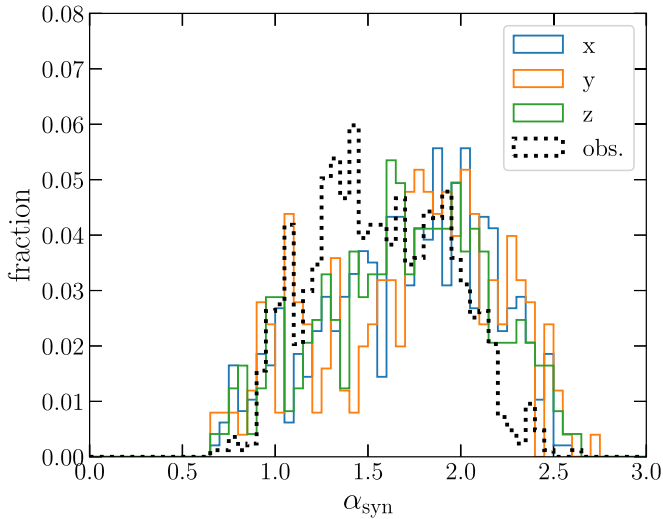
Figure 7. Distribution of spectral indices of the beams observable with the LOFAR sensitivity. The vertical axis shows the fraction of beams with each $\alpha_{\rm syn}$. The black dotted line shows the observation of Botteon et al. (2022). In our calculation, the total number of observable beams is ≈ 300 (30% of the area), while the observational data show the distribution of 836 pixels. For the model parameters, we adopted $\eta_B = 0.05$ and $\psi = 0.6$. The reacceleration is calculated for $T_{\rm dur} = 3$ Gyr, and the beam size is assumed to be 35". We tested the projection along three different axes (x, y, and z, distinguished by colors).

The value of $\eta_{\rm acc}$ (Equation (9)) differs from cell to cell, and it becomes $\eta_{\rm acc} \approx 0$ when $F_{\rm turb}$ is very small and the effect of the reacceleration is negligible. To obtain a typical value of $\eta_{\rm acc}$ in this model, we calculate

$$\eta_{\rm acc} = \frac{\sum(\frac{d\epsilon_{\rm CRe}}{dt} + \varepsilon_{\rm rad})}{\sum F_{\rm turb}}, \qquad (10)$$

where the sum is taken over the cells in each beam ($\sim 10^3$ cells). We calculate the mean value of $\eta_{\rm acc}$ for the 375 beams and find $\langle \eta_{\rm acc} \rangle \approx 1\%$. Although there is plenty of turbulent energy in cells with $F_{\rm turb} > 5 \times 10^{44}\,{\rm erg}\,{\rm s}^{-1}\,{\rm Mpc}^{-3}$, the occurrence of such cells is small (4.5%). The combination of those two results in $\eta_{\rm acc} \approx 1\%$, which is slightly smaller than that found in the one-zone model (Section 4.1).

Figure 7 shows the distribution of spectral index in each beam calculated with $\psi = 0.6$ and $\eta_B = 0.05$. The black dashed line shows the result reported in Botteon et al. (2022). The mean value of the index in our calculation is $\langle \alpha \rangle \approx 1.7$, and the difference in the results of three different projections is marginal. Our results are in line with the observation of diffuse radio emission enveloping A2255.

5. Limitations

Clearly, the complex morphology observed by LOFAR suggests that at least shocks and turbulence contribute to the emission. A full modeling of A2255, however, is beyond the aim of the present work. We have explored the possibility of turbulent reacceleration in the context of the specific model of Brunetti & Lazarian (2016). We find that the steep-spectrum diffuse emission observed at 1–2 Mpc from the center of A2255 can be explained using parameters (η_B and ψ) that are in line with previous literature (Brunetti & Lazarian 2016; Brunetti & Vazza 2020). In this case, the spatial diffusion coefficient of the CRes becomes $D \sim 10^{31}\,{\rm cm}^2\,{\rm s}^{-1}$ (Equation (3)), i.e., CRes can diffuse over 450 kpc within

1 Gyr. Within the acceleration time of radio-emitting CRes, $t_{\rm acc} \sim 500$ Myr (Equation (6)), the diffusion length is ~ 300 kpc. In addition, CRes can be spread and mixed by turbulent motion. This implies that CRes can travel ~ 30 cells during reacceleration, making the distribution smoother. Since the cells that efficiently accelerate CRs appear in every $\sim 3^3$ cell (i.e., $\sim 4\%$), the diffusion is fast enough to fill the space between turbulent cells.

We tested two cases: the one-zone model in Section 4.1 and the cell-wise calculation in Section 4.2. In the former case, we adopt the average values of the physical quantities found in the simulated box to calculate the FP equation. In the latter case, we neglected the transport during the short reacceleration and calculated the reacceleration using the local value of the turbulent flux in each cell. A future study with a Lagrangian tracer method will be important to discuss the evolution of the CR spectrum and spatial distribution due to the combination of reacceleration, spatial diffusion, and advection. An observation with higher angular resolution would also be important to study the correlation between the flat spectrum and large turbulent kinetic flux predicted in Section 4.2, or the gradient of the spectral index around the turbulent region due to the diffusion.

Concerning the initial condition, we have assumed that there is a cooling phase with $D_{pp} = 0$ before the reacceleration starts, as in many models of the giant radio halo (e.g., Brunetti et al. 2001; Nishiwaki & Asano 2022). However, CRs can be gently reaccelerated for several gigayears by the modest level of turbulence that is continuously driven by mass accretion. This would imply that there is no clear onset of the megahalo emission, unlike for classical halos, which are supposed to be driven by the mergers of clusters (e.g., Cassano et al. 2016). In Appendix B, we assume a different initial condition, i.e., that the reacceleration was working before the epoch of the snapshot. In this case, the observed emission can be explained by an efficiency that is slightly reduced, $\eta_{\rm acc} \approx 1.7\%$.

The tracer approach is also important for that issue. Following the energy gain and loss of CRes with a tracer method in a simulated galaxy cluster, Beduzzi et al. (2023) demonstrated that $\approx 22\%$–57% of the megahalo region ($0.4 R_{500} < r < R_{500}$) is filled with radio-emitting CRes. Although the details of the simulation setup and the definition of the volume filling factor are different from our study, their result suggests that the cluster-scale diffuse emission is produced through multiple episodes of turbulent reacceleration.

When extracting the peripheral region of the simulated cluster in Section 2, we choose the particular sector where large-scale accretion can be seen (Figure 1), motivated by the fact that the most turbulent region dominates the emission in our model (Section 4). We note that the typical turbulent energy can be smaller in other sectors without such an accretion feature. Considering that the properties of the gas and turbulence seen in the MHD simulation can be different from those in A2255, the parameters reported in this study are basically indicative values.

6. Conclusions

Recent LOFAR observations reported the presence of diffuse radio emission permeating the volume of galaxy clusters up to the virial radius. This emission is termed a megahalo, and its mechanism is still unclear.

The diffuse radio emission in A2255 has a very large extent, enveloping the example of classical halo and relics reported in

previous observations (e.g., Botteon et al. 2022). The complex radio morphology is likely generated through a mix of different processes, e.g., particle acceleration by shocks and turbulence. The diffuse emission permeating the cluster volume on large scales is a candidate for turbulent reacceleration. In this paper, we have explored this hypothesis.

Recent MHD simulations show that the turbulent energy is dominated by the solenoidal component in the cluster outskirts, so we focus on the acceleration mechanism presented by Brunetti & Lazarian (2016), where particles are accelerated by their interaction with magnetic field lines diffusing in a super-Alfvénic solenoidal turbulent flow. The acceleration efficiency D_{pp} depends on the mfp of a CR particle, $\psi \equiv \lambda_{\mathrm{mfp}}/l_A$, which is treated as a free parameter (Equation (2)).

We use a snapshot of a simulated cluster mimicking A2255 and study the properties of turbulence and magnetic field in the cluster outskirts. We extract a cubic volume of a region in the cluster periphery, where the prominent feature of mass accretion can be seen (Figure 1). Since the spatial resolution of the simulation is not sufficient to resolve the small-scale dynamo at the Alfvén scale, the magnetic field is estimated in a post-process. We assume that $\eta_B \approx 0.05$ of the turbulent flux is consumed as the dynamo and obtain $B \approx 0.2\,\mu\mathrm{G}$, which is roughly twice as large as the field found in the simulation. Comparing the efficiency of reacceleration and radiative cooling, we find that the diffuse emission in A2255 can be explained with a fiducial value of ψ (~ 0.5) that was derived from considerations based on mirroring of electrons in a super-Alfvénic flow (Brunetti & Lazarian 2016; Brunetti & Vazza 2020).

The emission spectrum is calculated by numerically integrating the FP equation (Equation (8)) with the quantities found in the MHD simulation. Before the reacceleration, CRes are accumulated around $p \sim 10^2$ due to the radiative and Coulomb cooling before the reacceleration. In Section 4.1, we adopted the one-zone approximation and used the average quantities in the simulation box. We find that the reacceleration by the solenoidal turbulence is efficient enough to produce a CRe spectrum peaked at $p \sim 10^4$, corresponding to a synchrotron frequency of $\sim 100\,\mathrm{MHz}$ in the $\sim 0.1\,\mu\mathrm{G}$ field. The acceleration efficiency is $\eta_{\mathrm{acc}} \approx 0.02$, in line with the estimate in Botteon et al. (2022).

We also calculate the FP equation in 10^6 cells in the simulation box, assuming that the seed CRes are uniformly distributed. We find that $100\,\mathrm{MHz}$ emission is dominated by the cells with large turbulent kinetic flux ($F_{\mathrm{turb}} > 5 \times 10^{44}$ erg s^{-1} Mpc^{-3}), which fill only a few percent of the volume. Considering the LOS integration within the beam size of LOFAR, we find that a large fraction of the beams ($\gtrsim 30\%$) can be detected with the LOFAR sensitivity. In this model, only 1% of the turbulent energy needs to be consumed for the particle acceleration in the turbulent cells. Our model predicts that the emission will be more volume-filling when observed with higher sensitivity at lower frequencies.

The reported parameters and the derived efficiencies are indicative values, as the simulations do not necessarily reproduce the turbulent properties of A2255. For this reason, our study simply suggests that there is room for turbulent reacceleration to contribute to the observed emission.

In reality, CRes in each cell would be mixed by the streaming and/or diffusion, although we neglect those effects in the current study. As discussed in Section 5, an mfp comparable to the Alfvén scale leads to a strong diffusion with $D \sim 10^{31}$ cm^2 s^{-1}, and CRes can diffuse over a few hundred kiloparsecs within ~ 1 Gyr. A method that can incorporate those effects, such as the application of a Lagrangian tracer method (e.g., Vazza et al. 2023), will be important for more accurate modeling.

Appendix A
Cosmic-Ray Protons and Secondary Electrons

In addition to the turbulent reacceleration, the injection of secondary leptons from the decay of pions produced by pp collisions between CRps and thermal protons is often invoked for the mechanism for the diffuse radio emission in galaxy clusters (e.g., Dennison 1980; Blasi & Colafran-cesco 1999; Keshet & Loeb 2010; Enßlin et al. 2011). The limits on the gamma-ray emission from the ICM (e.g., Jeltema & Profumo 2011; Ackermann et al. 2014, 2016) suggest that the contribution of secondary particle production through pp collisions to the observed emission is subdominant (Brunetti et al. 2017; Adam et al. 2021). However, the secondary leptons can contribute to the diffuse radio emission by providing the seed population for the reacceleration (e.g., Brunetti et al. 2017; Pinzke et al. 2017; Nishiwaki et al. 2021). Also, the minihalos in the dense core of cool-core clusters can originate from the injection of secondaries (e.g., Pfrommer & Enßlin 2004; Fujita et al. 2007; ZuHone et al. 2015; Ignesti et al. 2020). In this appendix, we explore the contribution of the secondary electrons to the diffuse emission found in cluster outskirts.

We calculate the injection of secondary CRes for a given distribution of CRps, using the procedure of Nishiwaki et al. (2021). We assume a single power-law spectrum of CRps, $N_p \propto p^{-\alpha_p}$, with $\alpha_p = 3.2$ to fit the radio synchrotron spectrum with $\alpha_{\mathrm{syn}} \approx 1.6$. We set $p/(m_p c) = 1$ for the minimum momentum of CRps. The energy density of CRps ϵ_{CRp} is treated as a free parameter. For simplicity, we neglect the reacceleration of both CRes and CRps. We adopt the one-zone approximation explained in Section 4.1.

In Figure 8, we show the energy densities of CRps and the magnetic field required to explain the observed brightness at $49\,\mathrm{MHz}$ in the pure hadronic model without reacceleration. We find that ϵ_{CRp} should be as large as $\epsilon_{\mathrm{CRp}} \approx 10^3 \epsilon_{\mathrm{ICM}}$ to explain the observed brightness when we adopt the same magnetic field
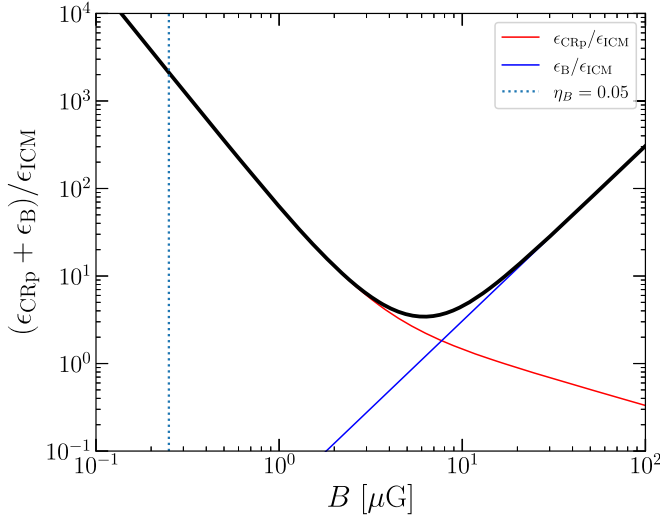
Figure 8. Energy densities of CRps and magnetic field required in the pure hadronic model without reacceleration as a function of the magnetic field. The red and blue lines show ϵ_{CRp} and ϵ_B, respectively. The thick black line shows the sum of those two. The energy densities are normalized by that of the ICM in the simulated box ($\epsilon_{ICM} = 1.3 \times 10^{-13}$ erg cm^{-3}). The spectral index of CRps is assumed to be $\alpha_p = 3.2$. The vertical dotted line shows the magnetic field calculated with $\eta_B = 0.05$ (Section 3).

as Section 4.1, i.e., $B = 0.24\,\mu\text{G}$. The energy density of secondary CRes is negligible compared to that of CRps. The synchrotron brightness scales as $S_{syn} \propto K_e B^{(\delta+1)/2}$, where $K_e \propto \epsilon_{CRp}/(B^2 + B_{CMB}^2(z))$ and $\delta \approx \alpha_p + 1$ are the normalization and the power-law index of the secondary CRe spectrum, respectively (e.g., Brunetti & Jones 2014). We find that the minimum value of the nonthermal energy density ($\epsilon_{CRp} + \epsilon_B$) is three times larger than ϵ_{ICM}, and it appears when the magnetic field is as large as $B = 6\,\mu\text{G}$. Thus, the classical "pure hadronic" model, which does not include any reacceleration, is incompatible with the observed megahalo.

Note that the above discussion does not exclude the possibility that the diffuse emission is produced by the reacceleration of the secondaries injected through pp collisions. A comprehensive study of this "secondary reacceleration" model should incorporate the reacceleration of CRps, which is beyond the scope of this work. It is worth noting that turbulence might be significantly damped by the back reaction of the reacceleration of CRps when $\epsilon_{CRp} \gtrsim \epsilon_{turb}$ (e.g., Brunetti & Lazarian 2007). Such a back reaction is not considered in the derivation of Equation (2).

Appendix B
Dependence on the Initial Condition

In Section 4, we assumed that the initial spectrum before the onset of the reacceleration, $N_e(p, 0)$, is determined by the radiative and Coulomb cooling. The spectrum has a peak around $p_{min} \sim 10$ as shown in Figure 5. However, it is also possible that the "initial spectrum" is affected by the turbulent reacceleration working before the time of the snapshot. Recent simulation by Beduzzi et al. (2023) observed that the radio-emitting CRes in the ICM experience multiple episodes of reacceleration. In such a case, the peak of the seed CRe spectrum should appear at a larger momentum $p_{min} \sim 10^2$–10^3. In this appendix, we discuss how the results in Section 4.2 are modified when we adopt a different initial spectrum. We adopt the same method as Section 4.2, taking into account the LOS integration. We also fix $\eta_B = 0.05$ here.

To consider the reacceleration before the epoch of the snapshot, we assume the initial spectrum for the calculation with $p_{min} = 10^3$. The shape of the initial spectrum is assumed to be the same in all cells. The initial energy density of the CRes follows $\epsilon_{CRe}(t = 0) \propto \epsilon_{ICM}$, as in Section 4.2.

The difference of the initial spectrum is not important when T_{dur} ((duration of reacceleration) is very long and the steady state due to the balance between the cooling and reacceleration is achieved in most of the cells. In Section 4, we find that the steady state is achieved at $T_{dur} \geqslant 3$ Gyr when $t_{acc} \approx 0.5$ Gyr.

In this appendix, we limit T_{dur} to $\approx 2t_{eddy}$, where t_{eddy} is the eddy turnover time measured in each cell. For the cells with $2t_{eddy} \gtrsim 1$ Gyr, we terminate the calculation at 1 Gyr. The mean value of t_{eddy} in the simulated box is ≈ 0.5 Gyr, so $T_{dur} = 2t_{eddy}$ is shorter than 3 Gyr in most of the cells.

With the above conditions, we find that the typical spectral index, $\alpha_{syn} \approx 1.6$, can be reproduced with $\psi = 0.5$. Figure 9 (right) shows the CRe spectra before and after the calculation. Summing up the CRe spectra over cells included in one beam ($\sim 10^3$ cells), we find that p_{min} after the calculation does not change much from the initial value, $p_{min} = 10^3$. This is consistent with the assumption that $p_{min} = 10^3$ is caused by the turbulent acceleration prior to the epoch of the snapshot. We calculate the acceleration efficiency using Equation (10) and find a typical value of $\langle \eta_{acc} \rangle \approx 1.7\%$.

Although we assumed a shorter T_{dur} than that in Section 4.2, the contribution of the cells with smaller turbulent energy ($F_{turb} < 5 \times 10^{44}$ erg s^{-1} Mpc^{-3}) increases, and almost 60% of the area of the emission region can be covered at the LOFAR sensitivity.
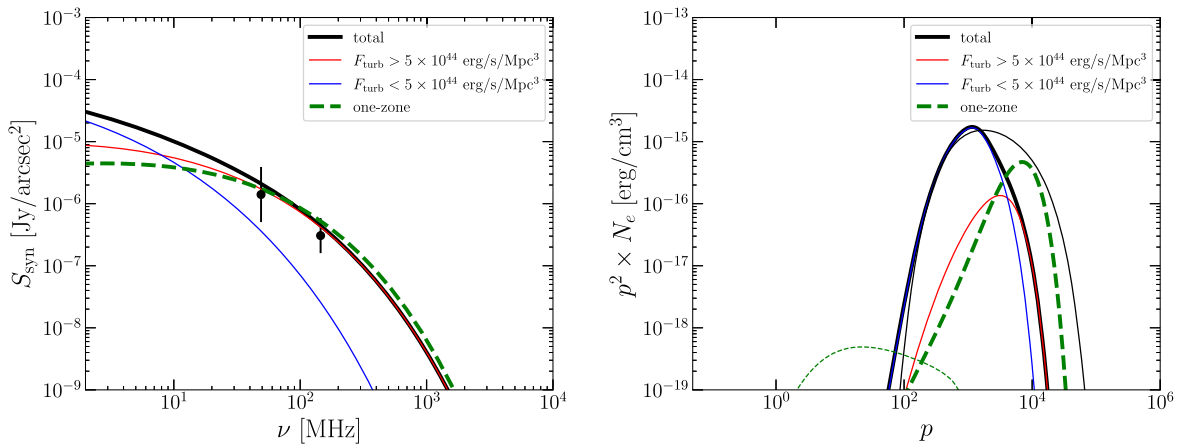
Figure 9. Same as Figure 5, but the minimum momentum of the initial spectrum is assumed to be $p_{\min}=10^3$ due to the reacceleration before the epoch of the snapshot. The duration of the FP calculation is limited by $2t_{\rm eddy}$, and $\psi=0.5$ is adopted.

If we adopt the initial spectrum with $p_{\min}\sim10$ and calculate reacceleration for $T_{\rm dur}=2t_{\rm eddy}$, the number of CRes with $p\sim10^4$ in the final state becomes smaller than in the $p_{\min}\sim10^3$ case and that model cannot explain the observed brightness unless $\eta_{\rm acc}\gtrsim10\%$.

ORCID iDs

Kosuke Nishiwaki https://orcid.org/0000-0003-2370-0475
Gianfranco Brunetti https://orcid.org/0000-0003-4195-8613
Franco Vazza https://orcid.org/0000-0002-2821-7928
Claudio Gheller https://orcid.org/0000-0003-1063-3541

References

Ackermann, M., Ajello, M., Albert, A., et al. 2014, ApJ, 787, 18
Ackermann, M., Ajello, M., Albert, A., et al. 2016, ApJ, 819, 149
Adam, R., Goksu, H., Brown, S., Rudnick, L., & Ferrari, C. 2021, A&A, 648, A60
Akamatsu, H., Mizuno, M., Ota, N., et al. 2017, A&A, 600, A100
Beduzzi, L., Vazza, F., Brunetti, G., et al. 2023, A&A, 678, L8
Beresnyak, A. 2012, PhRvL, 108, 035002
Beresnyak, A., & Miniati, F. 2016, ApJ, 817, 127
Blasi, P., & Colafrancesco, S. 1999, APh, 12, 169
Botteon, A., Brunetti, G., van Weeren, R. J., et al. 2020a, ApJ, 897, 93
Botteon, A., van Weeren, R. J., Brunetti, G., et al. 2020b, MNRAS, 499, L11
Botteon, A., van Weeren, R. J., Brunetti, G., et al. 2022, SciA, 8, eabq7623
Brunetti, G., & Jones, T. W. 2014, IJMPD, 23, 1430007–98
Brunetti, G., & Lazarian, A. 2007, MNRAS, 378, 245
Brunetti, G., & Lazarian, A. 2011a, MNRAS, 410, 127
Brunetti, G., & Lazarian, A. 2011b, MNRAS, 412, 817
Brunetti, G., & Lazarian, A. 2016, MNRAS, 458, 2584
Brunetti, G., Setti, G., Feretti, L., & Giovannini, G. 2001, MNRAS, 320, 365
Brunetti, G., & Vazza, F. 2020, PhRvL, 124, 051101
Brunetti, G., Zimmer, S., & Zandanel, F. 2017, MNRAS, 472, 1506
Bryan, G. L., Norman, M. L., O'Shea, B. W., et al. 2014, ApJS, 211, 19
Burns, J. O., Roettiger, K., Pinkney, J., et al. 1995, ApJ, 446, 583
Bustard, C., & Oh, S. P. 2022, ApJ, 941, 65
Cassano, R., & Brunetti, G. 2005, MNRAS, 357, 1313
Cassano, R., Brunetti, G., Giocoli, C., & Ettori, S. 2016, A&A, 593, A81
Cassano, R., Brunetti, G., Röttgering, H. J. A., & Brüggen, M. 2010, A&A, 509, A68
Cassano, R., Cuciti, V., Brunetti, G., et al. 2023, A&A, 672, A43
Cho, J., & Lazarian, A. 2006, ApJ, 638, 811
Cho, J., Vishniac, E. T., Beresnyak, A., Lazarian, A., & Ryu, D. 2009, ApJ, 693, 1449
Cuciti, V., de Gasperin, F., Brüggen, M., et al. 2022, Natur, 609, 911
del Valle, M. V., de Gouveia Dal Pino, E. M., & Kowal, G. 2016, MNRAS, 463, 4331
Dennison, B. 1980, ApJL, 239, L93

Domínguez-Fernández, P., Vazza, F., Brüggen, M., & Brunetti, G. 2019, MNRAS, 486, 623
Eckert, D., Ghirardini, V., Ettori, S., et al. 2019, A&A, 621, A40
Enßlin, T., Pfrommer, C., Miniati, F., & Subramanian, K. 2011, A&A, 527, A99
Feretti, L., Boehringer, H., Giovannini, G., & Neumann, D. 1997, A&A, 317, 432
Fujita, Y., Kohri, K., Yamazaki, R., & Kino, M. 2007, ApJL, 663, L61
Fujita, Y., Takizawa, M., & Sarazin, C. L. 2003, ApJ, 584, 190
Golovich, N., Dawson, W. A., Wittman, D. M., et al. 2019, ApJS, 240, 39
Govoni, F., Murgia, M., Feretti, L., et al. 2005, A&A, 430, L5
Govoni, F., Orrù, E., Bonafede, A., et al. 2019, Sci, 364, 981
Ignesti, A., Brunetti, G., Gitti, M., & Giacintucci, S. 2020, A&A, 640, A37
Jaffe, W. J., & Rudnick, L. 1979, ApJ, 233, 453
Jeltema, T. E., & Profumo, S. 2011, ApJ, 728, 53
Keshet, U., & Loeb, A. 2010, ApJ, 722, 737
Kowal, G., de Gouveia Dal Pino, E. M., & Lazarian, A. 2011, ApJ, 735, 102
Kowal, G., de Gouveia Dal Pino, E. M., & Lazarian, A. 2012, PhRvL, 108, 241102
Kravtsov, A. V., & Borgani, S. 2012, ARA&A, 50, 353
Kunz, M. W., Schekochihin, A. A., Cowley, S. C., Binney, J. J., & Sanders, J. S. 2011, MNRAS, 410, 2446
Lazarian, A., & Vishniac, E. T. 1999, ApJ, 517, 700
Lazarian, A., & Xu, S. 2021, ApJ, 923, 53
Lazarian, A., & Xu, S. 2023, ApJ, 596, 63
Lemoine, M. 2021, PhRvD, 104, 063020
Lynn, J. W., Quataert, E., Chandran, B. D. G., & Parrish, I. J. 2014, ApJ, 791, 71
Miniati, F. 2015, ApJ, 800, 60
Nelson, K., Lau, E. T., & Nagai, D. 2014, ApJ, 792, 25
Nishiwaki, K., & Asano, K. 2022, ApJ, 934, 182
Nishiwaki, K., Asano, K., & Murase, K. 2021, ApJ, 922, 190
Petrosian, V. 2001, ApJ, 557, 560
Pfrommer, C., & Enßlin, T. A. 2004, A&A, 413, 17
Pinzke, A., Oh, S. P., & Pfrommer, C. 2017, MNRAS, 465, 4800
Pizzo, R. F., & de Bruyn, A. G. 2009, A&A, 507, 639
Pizzo, R. F., de Bruyn, A. G., Feretti, L., & Govoni, F. 2008, A&A, 481, L91
Porter, D. H., Jones, T. W., & Ryu, D. 2015, ApJ, 810, 93
Press, W. H., & Schechter, P. 1974, ApJ, 187, 425
Ptuskin, V. S. 1988, SvAL, 14, 255
Schekochihin, A. A., Cowley, S. C., Dorland, W., et al. 2009, ApJS, 182, 310
Schekochihin, A. A., Cowley, S. C., Kulsrud, R. M., Hammett, G. W., & Sharma, P. 2005, ApJ, 629, 139
Schlickeiser, R., & Miller, J. A. 1998, ApJ, 492, 352
Steinwandel, U. P., Böss, L. M., Dolag, K., & Lesch, H. 2022, ApJ, 933, 131
Steinwandel, U. P., Dolag, K., Böss, L., & Marin-Gilabert, T. 2023, arXiv:2306.04692
van Weeren, R. J., de Gasperin, F., Akamatsu, H., et al. 2019, SSRv, 215, 16
Vazza, F., Brunetti, G., Brüggen, M., & Bonafede, A. 2018, MNRAS, 474, 1672

Vazza, F., Brunetti, G., Gheller, C., Brunino, R., & Brüggen, M. 2011, A&A,
     529, A17
Vazza, F., Jones, T. W., Brüggen, M., et al. 2017, MNRAS, 464, 210
Vazza, F., Wittor, D., Brüggen, M., & Gheller, C. 2016, Galax, 4, 60
Vazza, F., Wittor, D., Di Federico, L., et al. 2023, A&A, 669, A50

Xu, S., & Lazarian, A. 2016, ApJ, 833, 215
Yuan, Q., Zhou, X., & Jiang, Z. 2003, ApJS, 149, 53
ZuHone, J. A., Brunetti, G., Giacintucci, S., & Markevitch, M. 2015, ApJ,
     801, 146
ZuHone, J. A., Markevitch, M., & Lee, D. 2011, ApJ, 743, 16